ASME Journal of Heat and Mass Transfer
Online journal at:
https://asmedigitalcollection.asme.org/heattransfer

Ali Q. Abd Al-Hassan
Mechanical Engineering Department,
College of Engineering,
University of Basrah,
Basrah ■, Iraq

Muneer A. Ismael[1]
Mechanical Engineering Department,
College of Engineering,
University of Basrah,
Basrah ■, Iraq;
College of Engineering,
University of Warith Al-Anbiyaa,
Karbala ■, Iraq
e-mail: muneer.ismael@uobasrah.edu.iq

Mohammad Ghalambaz
Department of Mathematical Sciences,
Saveetha School of Engineering,
SIMATS,
Chennai ■, India;
Laboratory on Convective Heat and Mass Transfer,
Tomsk State University,
Tomsk 634045, Russia
e-mail: m.ghalambaz@gmail.com

Modeling of Rotating Frame Within a Cylindrical Vessel Containing Isothermal Cylinders Equipped With Flexible Radial Baffles

This study investigates the heat exchange within hot and cold cylinders in a cylindrical vessel featuring a rotating frame equipped with flexible baffles. The research examines the impact of cylinder size, proximity to the center, Rayleigh number, and rotational speed (ω). Flexible baffles are installed along the vessel walls to enhance mixing. The study employs the FE Method of rotating meshes to discretize and solve time-dependent equations. Findings reveal that using flexible baffles at a rotational speed of ω* = 50 leads to a 5.64% increase in the Nusselt number and a 56.9% decrease in the skin friction. Additionally, the research indicates thatleadncrease in both the rotational speed and the Rayleigh number leads to a corresponding increase in the Nusselt number. Specifically, the Nusselt number surges by 82.9% and 10.2% for $Ra = 10^5$ and 10^3, respectively, when ω* is raised from the rest to 200. Moreover, with a reduction in cylinder size to 0.01 radius, the Nu number boosts by 375.5% for $Ra = 10^5$ and 203.3% for $Ra = 10^3$, respectively. Moreover, the performance coefficient for flexible baffles, compared to rigid baffles, peaked at 92.48% at a rotation speed of 100 and $Ra = 10^5$.* [DOI: 10.1115/1.4068791]

Keywords: mixing mechanism, rotating frame, cylinders, rotational mesh, FSI

1 Introduction

Rotating frames, or cylinders of various shapes, possess vital significance in numerous industrial applications such as electronic cooling systems, nuclear and chemical reactors, and heat exchangers [1–3]. Circulating heat transfer fluid between bundles of cylinders is the significant demand for improving heat transfer in nuclear reactors [1]. The influence of rotating cylinders on heat transfer has been extensively explored in several studies. Ghaddar and Thiele [4] analyzed two-dimensional convectional heat transfer from a rotating cylinder in the center of an isothermal rectangular enclosure, noting improved heat transfer with rotation. They observed that under low Rayleigh number to rotational Reynolds number ratios, the maximum cylinder surface temperature could drop by 25–35% compared to stationary cylinders.

Experimental and numerical studies conducted by Kimura et al. [5] focused on the combined convection in a cavity using a centrally rotating plate. Paramane and Sharma [6] suggested that rotating a heated circular cylinder could effectively suppress heat transfer based on their two-dimensional numerical analysis of forced convection. Costa and Raimundo [7] found that rotating cylinders within enclosures significantly affect thermal performance, with the cylinder's thermophysical properties dictating the heat transfer dynamics.

Other studies have shown that placing a rotating cylinder within a cavity could control heat transfer rates [8]. Liao and Lin [9] used numerical methods to demonstrate that cylinder rotation could diminish heat transfer. Chatterjee et al. [10] focused on moving wall cavities involving an adiabatic cylinder rotates within a nanofluid, underscoring the pivotal role of rotational speed in heat transfer efficiency. Atanasova et al. [11] investigated the fluid dynamics issues related to the process of accelerating from a stationary state (spin-up) and decelerating to a stationary state (spin-down). The reported results can be used to devise a tailored rotation pattern for the bioreactor to enhance the mixing performance during the cell expansion phase. Mokhefi [12] conducted a numerical analysis of the hydrodynamic characteristics of a Bingham fluid, which was used as a food ingredient in a mechanically agitated tank with an angled anchor. The study investigated both isothermal and non-isothermal conditions. It was discovered that using an angled anchor arrangement improves the axial flow in the agitated tank compared to typical setups while retaining the dominance of tangential flow. Yin et al. [13] focused on investigating the mixing process of hot and cold fluids in T-junctions, which is crucial for assuring the safe operation of T-junction pipe systems. An impeller is introduced into T-junction ducts, and experiments are performed utilizing particle image velocimetry without considering the temperature disparity between the two fluids. Blade tip vortex shedding was detected in the bottom section of the impeller. The jet flow pattern changed at high momentum ratios as the impeller rotated at various angles.

Considering industrial applications, several studies have explored the effects of rotating frames and fixed baffles. Karcz and Major [14]

[1]Corresponding author.

Contributed by the Heat Transfer Division of ASME for publication in the Journal of Heat and Mass Transfer. Manuscript received February 21, 2025; final manuscript received May 16, 2025; published online xx xx, xxxx. Assoc. Editor: Igor Shevchuk.

investigated how baffle length influences power consumption in vessels with short baffles, noting a significant relationship between baffle length and the turbulence of fluid flow, which in turn affects the power number. Similarly, Promvonge et al. [15] investigated the thermal-fluid fields in a channel with 45 deg tilted baffles on one wall, observing better performance than 90 deg baffles at various Reynolds numbers and baffle heights. Sriromreun et al. [16] compared the thermal performance in a rectangular channel with Z-baffles to one without baffles, both numerically and experimentally, highlighting enhanced heat transfer and friction with baffles. Xia et al. [17] investigated the flow interferences that arise in a twin-impeller stirring tank. These interferences occur among the paddles, the paddles-baffles, and the tank as the wall. These interferences destruct the utilization of the energy of stirring. The main goal of their study was to improve the efficiency and uniformity of mixing in tanks that combine solid and fluid substances while also reducing energy consumption and cost. The findings provide valuable information that can be applied to constructing comparable mixing tanks.

Due to its broad utility, the fluid–structure interaction (FSI) approach has increasingly become a focal point across various engineering fields, such as mechanical, aerospace, and biomedical engineering [18]. This methodology is applied in numerous scenarios, such as fluid flow through elastic pipes, operation of diaphragm pumps, piston movements in elastic chambers, functionality of diaphragm sensors, and the dynamics of blood flow in vessels [19]. Several studies have highlighted this method's versatility. Shi and Khodadadi [20] investigated the effects of a reciprocating fin protruding from a vertical wall of an enclosure, manifesting a moving wall. Meanwhile, Gomes and Lienhart [21] analyzed the FSI in turbulent and laminar flows affected by oscillating flexible assemblies. Ku [22] was awarded a patent for an innovative, flexible heat sink design. Further research by Soti et al. [23] demonstrated that the flow-induced deformation of a flexible oscillator could enhance heat transfer. Chamkha et al. [24] explored how an excited flexible fin affects heat transfer in an enclosed space and found that a horizontal excited fin does not markedly improve convection. Saleh et al. [25] investigated the impact of double-excited flexible fins on the transient convective heat transfer within partially porous layers confined by a square enclosure. Mahmood et al. [26] studied the phenomenon of pulsing heat transfer in a horizontal channel heated from its two horizontal walls and equipped with a flexible modulator. They found that the modulator tip's frequency coincides with the flow's pulsating frequency. Furthermore, the flexible modulator enhances heat transmission by enhancing flow mixing. Roy et al. [27] investigated the thermal efficiency of a power-law fluid in a moving wall enclosure with discrete heating. Their numerical result predicted the optimal heat transfer medium for a specific design, minimizing extra costs associated with conducting experiments. The study demonstrated a positive correlation between the index of the power-law and Nu in forced and mixed convection. Mahmood et al. [28] studied the combined convection features caused by fluid–structure interaction (FSI) in a square enclosure consisting of a power-law fluid. This study demonstrates that incorporating a flexible fin improves heat transmission exclusively at elevated Richardson numbers. Therefore, their system, which included non-Newtonian fluids and fin attachments, is primarily suited for situations where natural convection is the dominant factor.

Moreover, entropy generation, a key measure of thermal system performance, was also studied. Reasons for entropy production in applied thermal engineering are extensively discussed in various works [29–33] covering enclosures involving a still or rotating objects.

The review of existing studies highlights plenty of researches on natural convection heat transfer in several geometrical configurations and with different internal obstacles. However, the rotational dynamics of noncircular shapes have not been extensively explored. Such oversight is primarily due to the complexities in modeling the rotation of asymmetric objects, which often require advanced techniques like moving or deformed mesh methods or a combination of fixed-rotating frame strategies.

Our latest research [34] introduced an innovative technique to address the simulation of a rotating frame inside a circular enclosure encompassing a bundle of hot and cold cylinders. This study investigates the use of flexible baffles acting as a guide to the circulated fluid within a cylindrical enclosure involving hot and cold cylinders. This study, therefore, stands out by using the same fixed-rotating frame strategy and the FSI technique to simulate the conjugate heat transfer and mixed convection processes. Along with the Nusselt number, the skin friction is implemented to evaluate the role of the flexible baffles in enhancing heat transfer. The modeling and specific geometry used in this study are highly applicable to optimizing systems in various industrial sectors, including chemical plants, biological reactors, and nuclear reactor heat exchangers.

2 Mathematical Formulation

Figure 1 illustrates the setup of this study, which includes a vessel with a radius (R) and a conductive frame. The frame's dimensions are defined as $a \times b$ where $a = R$ and $b = 0.12R$, and R is the radius of the circular enclosure. The heat capacity and thermal conductivity ratios between the frame and the fluid are R_h and Rt_h, respectively. Positioned centrally, the rectangular frame rotates counterclockwise at a speed (ω). Along the vessel's periphery, cylinder bundles are placed, through which hot fluid flows, maintaining a constant surface temperature (T_h) on the cylinders. The vessel's outer surface is insulated to prevent heat loss. In this configuration, the cylinder angles are static, with four hot cylinders located in the lower half at angles of 202.5 deg, 247.5 deg, 292.5 deg, and 337.5 deg.

Conversely, in the upper half, four cold cylinders were located at angles of 22.5 deg, 67.5 deg, 112.5 deg, and 157.5 deg, with an interval of 45 deg between consecutive cylinders. Cold fluid flows through these cylinders, keeping their surface temperature constant at (T_c). Water fills the vessel with a Prandtl number of $\mathrm{Pr} = 6.90$. Eight flexible baffles were uniformly distributed along the surface of the cylinder. Each flexible baffle was positioned between two adjacent cylinders, with an angular separation of 22.5 deg from the center of each cylinder and 45 deg between consecutive baffles. The length and width of each baffle were denoted by ($a_{\mathrm{fl.}} = 0.12\,R$) and ($b_{\mathrm{fl.}} = 0.002\,R$), respectively. The ratio of thermal conductivities between the solid material (flexible baffles) and the fluid is represented by the dimensionless parameter k_r, which was calculated to be 13. The no-slip boundary condition is applied to all walls, including the flexible baffles' walls. Considering horizontal assembly, the variations along the z-axis are ignored; hence, the problem can be solved in a two-dimensional x–y plane. The Boussinesq approximation is utilized, relating density to temperature and incorporating the body force accordingly.

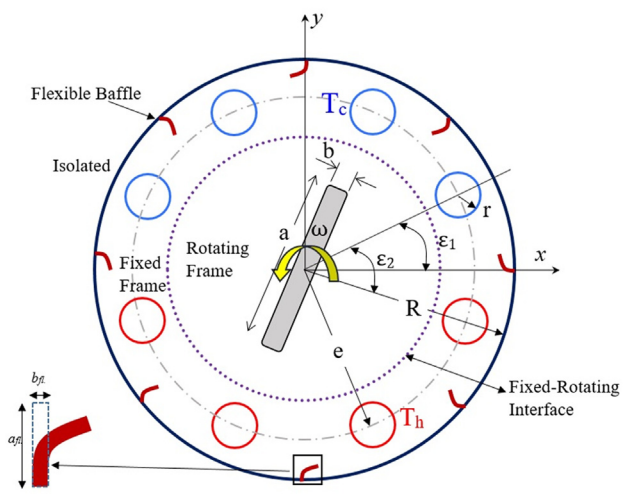

Fig. 1 Diagram and coordinate system of the analyzed scenario

By limiting the rotation speed of the frame to low values, laminar flow can be safely assumed. Moreover, the assumptions of incompressible fluid (water); constant fluid properties (except density); no heat dissipation, and a long horizontal cylindrical vessel led to no variation in the z-direction; making it a 2D problem. These assumptions simplify the numerical solution while maintaining the required accuracy. Hence, fundamental conservation equations can describe velocity and temperature fields in a rotating frame for an unsteady-state [35–38].

$$\nabla.\mathbf{W} = 0 \tag{1}$$

$$\rho\frac{\partial \mathbf{V}}{\partial t} + \rho\nabla.(\mathbf{W}_{co} \otimes \mathbf{V}) + \rho(\boldsymbol{\omega} \times \mathbf{V}) + \nabla p = \nabla.(\mu\nabla\,\mathbf{V}) + \mathbf{F}_b \tag{2}$$

$$\rho C_p\frac{\partial T}{\partial t} + \rho C_p\nabla.(\mathbf{W}_{co}\,T) = \nabla.(k\nabla\,T) \tag{3}$$

$$(\rho C_p)_s\frac{\partial T_s}{\partial t} = \nabla.(k_s\nabla\,T_s) \tag{4}$$

where $\mathbf{F}_b = \rho_0 g\beta(T - T_c)j$ and ω represent the angular velocity of the frame. Additionally, the absolute velocity $\mathbf{V}$ is defined as $\mathbf{V} = \mathbf{W} + \boldsymbol{\omega} \times \mathbf{r}$ in which $\mathbf{W}$ indicates the relative velocity, and $\boldsymbol{\omega} \times \mathbf{r}$ denotes the velocity due to the rotating frame. Moreover, $(\mathbf{W}_{co} = \mathbf{W} - \mathbf{W}_{fl})$, $\mathbf{W}_{fl}$ is the velocity of the moving coordinates.

For flexible baffle

The equation for momentum, which governs the nonlinear displacement of the flexible baffle, is expressed as follows:

$$\rho_{fl}\frac{\partial^2 d_{fl}}{\partial t^2} - \nabla\sigma = \mathbf{F}_{b(fl)} \tag{5}$$

The energy equation of the baffle

$$\frac{\partial T}{\partial t} = \alpha_{fl}\nabla^2 T \tag{6}$$

where $\mathbf{F}_{b(fl)}$ represents the body force exerted on the baffles given by $\mathbf{F}_{b(fl)} = \rho_{fl}\,g_y$. Here, d_{fl} indicates the displacement vector, σ the stress tensor, and α_{fl} the flexible baffles' thermal diffusivity.

The elastic displacement of the baffle, caused by the forces exerted by the fluid and pressure, can be described using the Kirchhoff stress tensor, as outlined in Ref. [39]

$$\tau_{fl} = J\,\sigma \tag{7}$$

$$\sigma = J^{-1}FZF^T \tag{8}$$

where $F = (1 + \nabla d_{\mathrm{fl}})$, $J = \det(F)$, J is Jacobin determent, τ is extra stress tensor, Z signifies the second Piola–Kirchhoff stress tensor, which correlates with the strain ε_{fl} by $Z = C : (\varepsilon)$ where $\varepsilon_{fl} = \frac{1}{2}(\nabla d_{fl} + \nabla d_{fl}{}^T + \nabla d_{fl}{}^T\nabla d_{fl})$where $C = C(E, \vartheta)$, C represents the elasticity tensor, ε denotes the strain rate, E shows the elastic modulus, ϑ indicates the Poisson ratio, and ":" signifying the double–dot tensor product.

The following dimensionless parameters are introduced:

$$\begin{aligned}
&\nabla^* = \frac{\nabla}{D},\ (e^*, r^*) = \frac{(e, r)}{D},\ \theta = \frac{T - T_c}{T_h - T_c},\ \omega^* = \frac{\omega D^2}{\alpha_f},\\
&\mathbf{V}^* = \frac{\mathbf{V}\,D}{\alpha_f},\ \mathbf{W}^* = \frac{\mathbf{W}\,D}{\alpha_f},\ \mathbf{W}^*{}_{\mathrm{co}} = \frac{\mathbf{W}_{co}\,D}{\alpha_f},\ t^* = \frac{(t\,\alpha_f)}{D^2},\\
&\mathrm{Ra} = \frac{g\beta D_h^3(T_h - T_c)}{\vartheta\,\alpha_f},\ p^* = \frac{(p + \rho_0 gy)}{\left(\rho_f\left(\alpha_f/D\right)^2\right)},\ \mathrm{Pr} = \frac{\vartheta}{\alpha_f},\\
&\sigma^* = \frac{\sigma}{E},\ E^* = \frac{E\,D^2}{\rho_f\alpha_f{}^2}
\end{aligned} \tag{9}$$

The collection of conservation equations has been reformulated as indicated in [40]

$$\nabla^*.\mathbf{W}^* = 0 \tag{10}$$

$$\frac{\partial \mathbf{V}^*}{\partial t^*} + \nabla^*.(\mathbf{W}^*{}_{\mathrm{co}} \otimes \mathbf{V}^*) + (\boldsymbol{\omega}^* \times \mathbf{V}^*) + \nabla^* p^* = \mathrm{Pr}\,\nabla^{*2}\mathbf{V}^* + \mathbf{F}_b^* \tag{11}$$

$$\frac{\partial \theta}{\partial t^*} + \mathbf{W}^*{}_{\mathrm{co}}\,\nabla^*\theta = \nabla^{*2}\theta \tag{12}$$

$$\frac{(\rho C_p)_s}{(\rho C_p)_f}\frac{\partial \theta_s}{\partial t^*} = \left(\frac{k_s}{k_f}\right)\nabla^{*2}\theta \tag{13}$$

where ω represents the solid frame's angular velocity and $\mathbf{F}_b^* = j\mathrm{Ra} \times \mathrm{Pr}\,\theta$.

The ratios R_{th} and R_h account for the ratios of thermal conductivity of the rotating frame to that of the fluid, and the heat capacity of the frame to that of the fluid, respectively, and they are expressed as

$$R_{\mathrm{th.}} = \frac{k_s}{k_f} \text{ and } R_h = \frac{(\rho c_p)_s}{(\rho c_p)_f} \tag{14}$$

For flexible baffles

$$\frac{1}{\rho_r}\frac{d^2 d_{\mathrm{fl}}{}^*}{dt^{*2}} - E^*\,\nabla\sigma^* = E^*\mathbf{F}^*{}_{b(\mathrm{fl})} \tag{15}$$

$$\frac{\partial \theta}{\partial t^*} = \alpha_r\nabla^2\theta \tag{16}$$

where $\rho_r = \frac{\rho_f}{\rho_{\mathrm{fl}}}$ and $\alpha_r = \frac{\alpha_{\mathrm{fl}}}{\alpha_f}$ are the ratios of the density and thermal diffusivity of the fluid to that of the flexible baffles, respectively.

Temperature boundary conditions for the vessel, expressed in dimensionless form, can be expressed as

$\theta = 1$, For the four heated cylinders in the lower part of the vessel (17*a*)

$\theta = 0$, For the four cold cylinders in the topper part of the vessel (17*b*)

$\frac{\partial \theta}{\partial n} = 0$, For the insulated outer surface of the vessel (17*c*)

$\theta_s = \theta_f$, The boundary conditions at the outer edge of the rotating frame (17*d*)

$$\left(\frac{\partial \theta}{\partial n}\right)_f = R_{th}\left(\frac{\partial \theta}{\partial n}\right)_s \tag{17e}$$

$\frac{\partial d_{fl}{}^*}{\partial t^*}\mathbf{W}^*$, $E^*\sigma.n = -p^* + \mathrm{Pr}\,\nabla\,\mathbf{W}^*$, For nonslip boundary conditions on the baffles (17*f*)

$\frac{\partial \theta_f}{\partial n} = k_r\frac{\partial \theta_{fl}}{\partial n}$, The The interface between flexible baffles and fluid (17*g*)

where $k_r = \frac{k_{fl}}{k_f}$ is the thermal conductivity ratio between flexible baffles and fluid.

To identify whether convection or conduction is the predominant, the Nusselt number at the hot cylinders is employed. Moreover, the skin friction C_{fr} along the vessel wall is used to evaluate the overall performance

$$\mathrm{Nu} = -\frac{1}{2\pi r}\int_0^{2\pi r}\left(\frac{\partial\theta}{\partial n}\right)dS \tag{18a}$$

$$C_{\mathrm{fr}} = \frac{1}{2\pi r}\int_0^{2\pi r}\left(\frac{\mathbf{W}^*}{\partial n}\right)dS \tag{18b}$$

In assessing the feasibility of the heat transfer process for this specific problem, it's crucial to compute a performance criterion. This criterion is determined by taking the ratio of the Nusselt number with flexible baffles to that without baffles and then dividing this result by the ratio of the skin friction coefficient with flexible baffles to that without baffles. This measure offers a dependable gauge of system efficiency and facilitates accurate comparisons

$$\mathrm{Pf} = \frac{\mathrm{Nu_{baf}}/\mathrm{Nu}_o}{C_{\mathrm{frbaf}}/C_{\mathrm{fr}o}} \tag{18c}$$

where the subscript "o" denotes without baffles and baf denote fixed or flexible baffles.

Another dimensionless number, represented by the power consumption (Ne) is presented in the following equation:

$$\mathrm{Ne} = \frac{\mathrm{Po}}{\omega i^3\, Di^5\, \rho} \tag{19a}$$

where

$$Po = 2\pi\, \omega i\, Mt \tag{19b}$$

3 Numerical Solution

The central circular enclosure and the flexible baffles are segmented into infinitesimal areas, and the finite element method (FEM) is employed to break down Eqs. (10)–(16). This method uses nonlinear residual equations formulated by weighting the residuals, commonly called Galerkin equations. These equations are applied across the domain, except in regions with cylindrical obstructions, facilitating accurate modeling of straight and curved boundaries. Basis functions are utilized to calculate unknown variables at each node of the elements, enabling the interpolation of temperature, pressure, and velocity

$$\text{the } u^*, v^* \approx \sum_i^M (u^*, v^*)_i^k \Phi_i^k(x^*, y^*),\ \ \theta \approx \sum_i^M \theta_i^k \Phi_i^k(x^*, y^*),$$
$$p^* \approx \sum_i^M p^{*k}_i \Phi_i^k(x^*, y^*) \tag{20}$$

In this formulation, i is the node index, M is the number of nodes, and k denotes the time-step iteration. PARDISO (parallel direct solver) is invoked to handle large sparse linear systems [41–45]. PARDISO is a fast, thread-safe library for solving large sparse linear systems on multicore machines Schenk and Gartner [46]. Using C language, it utilizes an efficient supernodal Gaussian elimination method, ideal for finite element and optimization problems. The solver was called as a C library to simulate the model. The mesh displacement, solid structure, heat transfer, and momentum equations were solved in a fully coupled format using the Newton method with a damping factor of 0.8 for better solution stability. The maximum iterations for each time-step were 200. Crosswind stabilization and second-order upwind approaches are utilized to overcome numerical convergence issues raised by diffusive and convective terms. The time-step is maintained at maximum of 10^{-3} s. The backward differentiation formula (BDF) of second order was used to adjust the time steps within the required relative error of 5×10^{-3}. Figure 2 demonstrates the FEM methodology, detailing the numerical procedures. Two precise computational analyses show that the error range remains within 5×10^{-3}

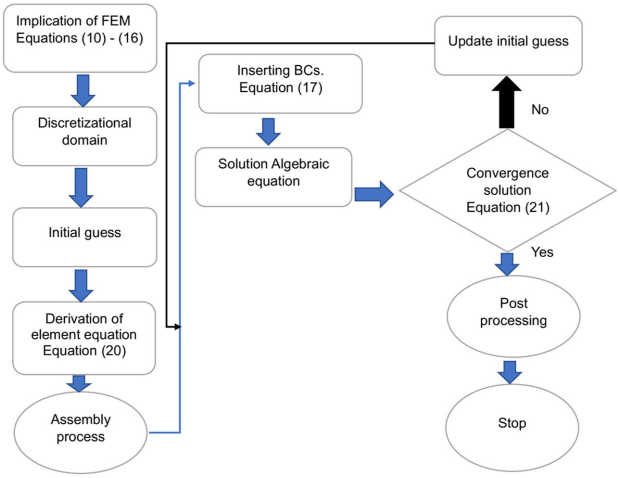

Fig. 2 Outlines of the FEM procedure

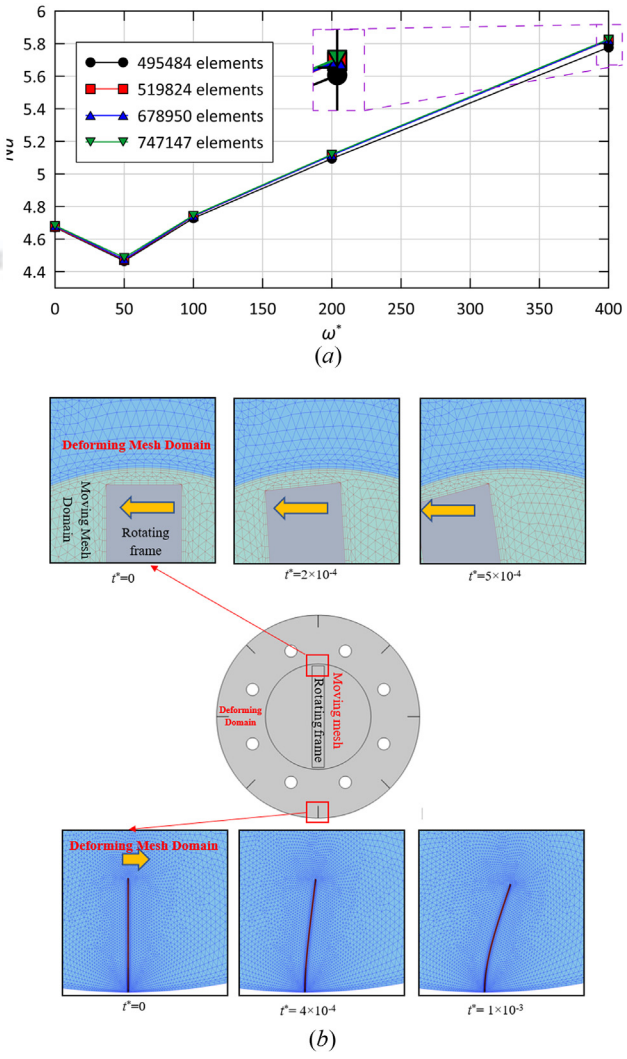

Fig. 3 (*a*) Grid independence test at $r^* = 0.03$, $e^* = 0.35$, and $\mathrm{Ra} = 10^3$ for different values of ω^* and (*b*) the finalized mesh, consisting of 519,824 elements zoomed to illustrate the mesh movement flexible baffle's motion

$$\left|\frac{\Gamma^{j+1}-\Gamma^{j}}{\Gamma^{j+1}}\right| \leq 5\times 10^{-3} \tag{21}$$

Γ can be pressure, temperature, or velocity, and iteration number is denoted by j. Following the substitution of equations, two primary procedures are executed during the numerical analysis phase. Initially, a proper mesh configuration is established, and the domain is segmented through an automated algorithm for mesh generation. Thereafter, comparisons with existing researches are conducted to ascertain the accuracy of the results, as further described in the subsequent sections.

AQ7

3.1 Verification of Grid Refinement. The convergence assessment in a vessel containing cylinders, each with a radius of $r^* = 0.03$, involves evaluating the temperature contours, streamlines, and Nusselt number. These cylinders were positioned away from the center of the enclosure center at $e^* = 0.35$ undergoing a frame rotation ranging from $\omega^* = 0$–400 at a Rayleigh number of 10^3 and Prandtl number of Pr = 6.9. The arrangement consists of four cold cylinders positioned at angles of $\varepsilon 1 = 22.5$ deg, 67.5 deg, 112.5 deg, and 157.5 deg. The hot cylinders are positioned at angles of $\varepsilon_1 = 202.5$ deg, 247.5 deg, 292.5 deg, and 337.5 deg, with an interval of $\varepsilon_2 = 45$ deg. The heat capacity ratio (R_h) and the conductivity ratio (R_{th}) between the frame and the fluid stay constant at 0.582 and 397.63, respectively. The inside surface of the vessel is equipped with eight flexible baffles, with Young's modulus (dimensionless) at $E^* = 2 \times 10^{10}$ and thermal conductivity ratio $k_r = 13$. The material of the flexible baffle was chosen to be a composite polymer (expanded graphite/polyetherimide (EG/PEI) composite) [47] with a thermal conductivity of 7.8 W/m.K, which is divided by the thermal conductivity of fluid water (0.6 W/mK), resulting in a kr value of 13. The nondimensional Young's modulus of $E^* = 2 \times 10^{10}$ is also in the range of expanded graphite/polyetherimide with specific mechanical processing. Various mesh sizes were analyzed, as shown in Fig. 3(*a*), with an optimal mesh size of 519,824 elements (depicted in Fig. 3(*b*)) chosen to meet accuracy and the time of solution. The specifications of this mesh are as follows; the minimum element quality is 0.1627, with an average quality of 0.8607, the element area ratio is 0.001524. Close to the interface

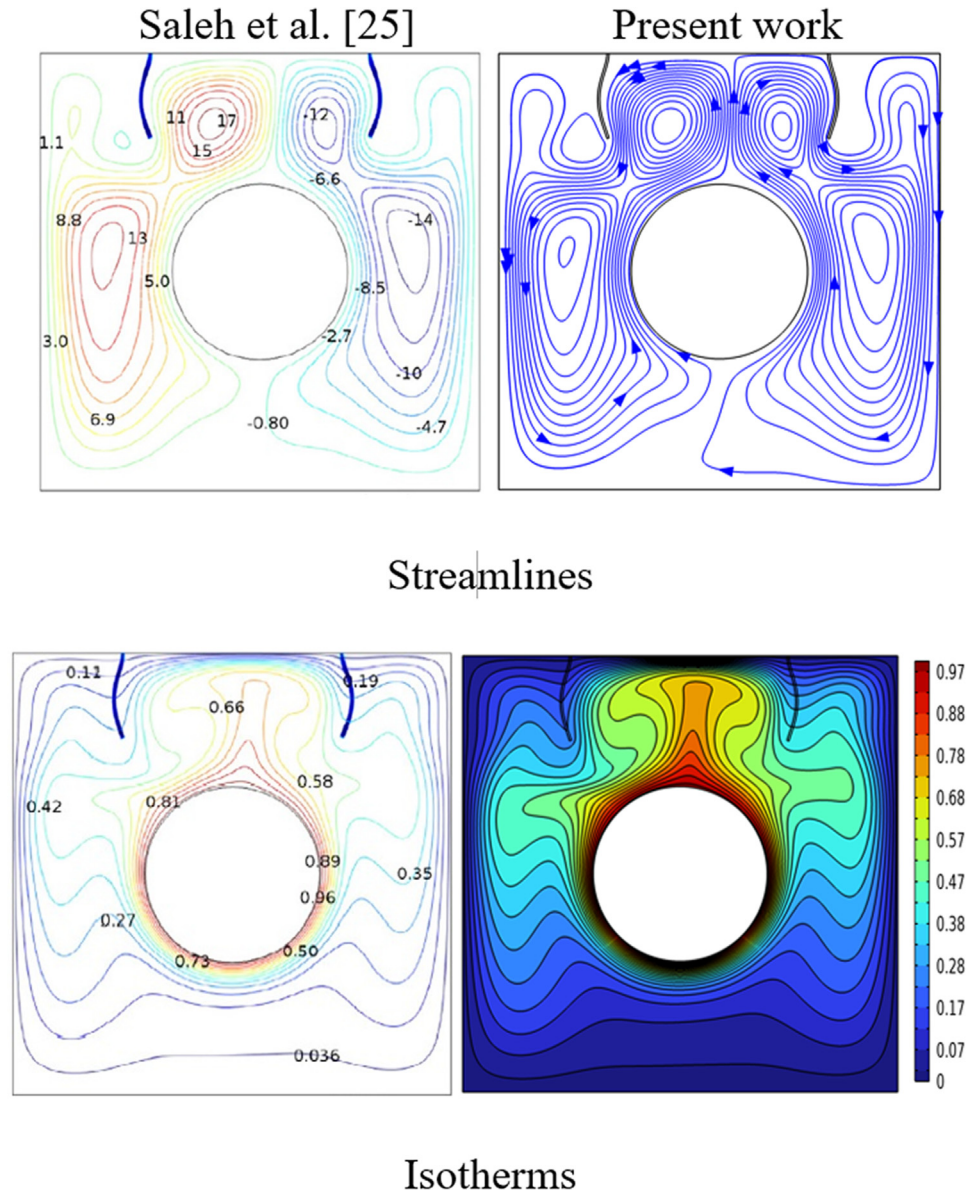

Fig. 4 Comparison with Saleh et al. [25], at the length of the fin ($a^* = 0.2$), elastic modulus ($E^* = 10^9$), oscillation amplitude ($A^* = 0.1$), the radius of cylinder ($R^* = 0.2$), Ra = 10^6 and oscillation period ($t_p^* = 0.5$) with $t^* = 1.125$ (4 t_p^*/8)

boundaries, the mesh is denser, while within the regular domains, less dense mesh is set. Skewness around the deflected baffles was also monitored and remained within acceptable limits throughout the simulation. The moving mesh is applied in the FSI part of the domain, i.e., close to the flexible baffles. Since the deflection of the flexible baffles was not significant, the distortion of the mesh was not so steep, where the mesh inversion was not encountered within the whole calculations. The figure illustrates the mesh movement within the rotating domain, where the mesh adjusts dynamically as the rotating frame moves while the other domain undergoes deformation. Furthermore, Fig. 3(*c*) displays the motion of the flexible baffles at three-time samples within the deformation domain, driven by the transfer of movement from the rotating frame.

3.2 Verifications of Results. To ensure the precision of the numerical method and achieve optimal outcomes, a validation test was conducted based on the research undertaken by Saleh et al. [25]. This investigation explored unsteady combined convection in an enclosure encompassing a hot circular cylinder, enhanced by two solid, thin, elastic baffles mounted on the upper cold wall, each with a length of L. The parameters evaluated in this study covered the oscillation's direction, amplitude, and length of the fins alongside various elasticity ratings and cylinder dimensions for fixed values of $\mathrm{Ra} = 10^6$ and $\mathrm{Pr} = 0.7$ (for air). A radius of R characterized the cylinder. The comparison yielded exceptional results, as indicated by the visualization of isotherms and streamlined contours, as shown in Fig. 4.

Furthermore, the comparison was conducted with the results of Ghaddar and Thiele [4], who utilized two-dimensional laminar flow within an enclosure measuring five in length and three in width. A circular rotating cylinder was employed, at a height of 1.5 from the base. The rotating cylinder was subjected to a uniform heat flux; meanwhile, the remainder of the enclosure was assumed to be isothermal. In both scenarios, the Ra number was 10^4, and the Pr number was set to unity. However, the rotational Reynolds number varied from zero for the stationary cylinder and 15.811 for the rotating cylinder. In the first scenario, with the cylinder stationary, and in the second scenario, with the cylinder rotating, the comparison of streamlines and isothermal produced excellent results, as shown in Figs. 5(*a*) and 5(*b*).

Further corroboration of the present methodology was achieved by juxtaposing it with experimental data. Karcz and Major's [14] experiment used a stirred water tank with an internal radius of 0.3 m. The tank was equipped with a 0.198-m (in diameter) Rushton turbine and was positioned 0.198 meters from the bottom of the vessel. They focused on turbulent flows within the vessel, particularly exploring Reynolds numbers ($\mathrm{Re} = \frac{\omega i \mathrm{Di}^2 \rho}{\mu}$) between 30,000 and 200,000. The study incorporated dimensionless equations along the (κ–ϵ) model to assess power consumption related to various Reynolds numbers. Figure 6 displays hopeful outcomes, bolstering confidence in numerical methods.

Extra validation regarding the FSI is conducted with the problem of Küttler and Wall [48], which composed a ported cavity having a base made of flexible material ($E = 250\ \mathrm{N/m^2}$) while the lid moves in

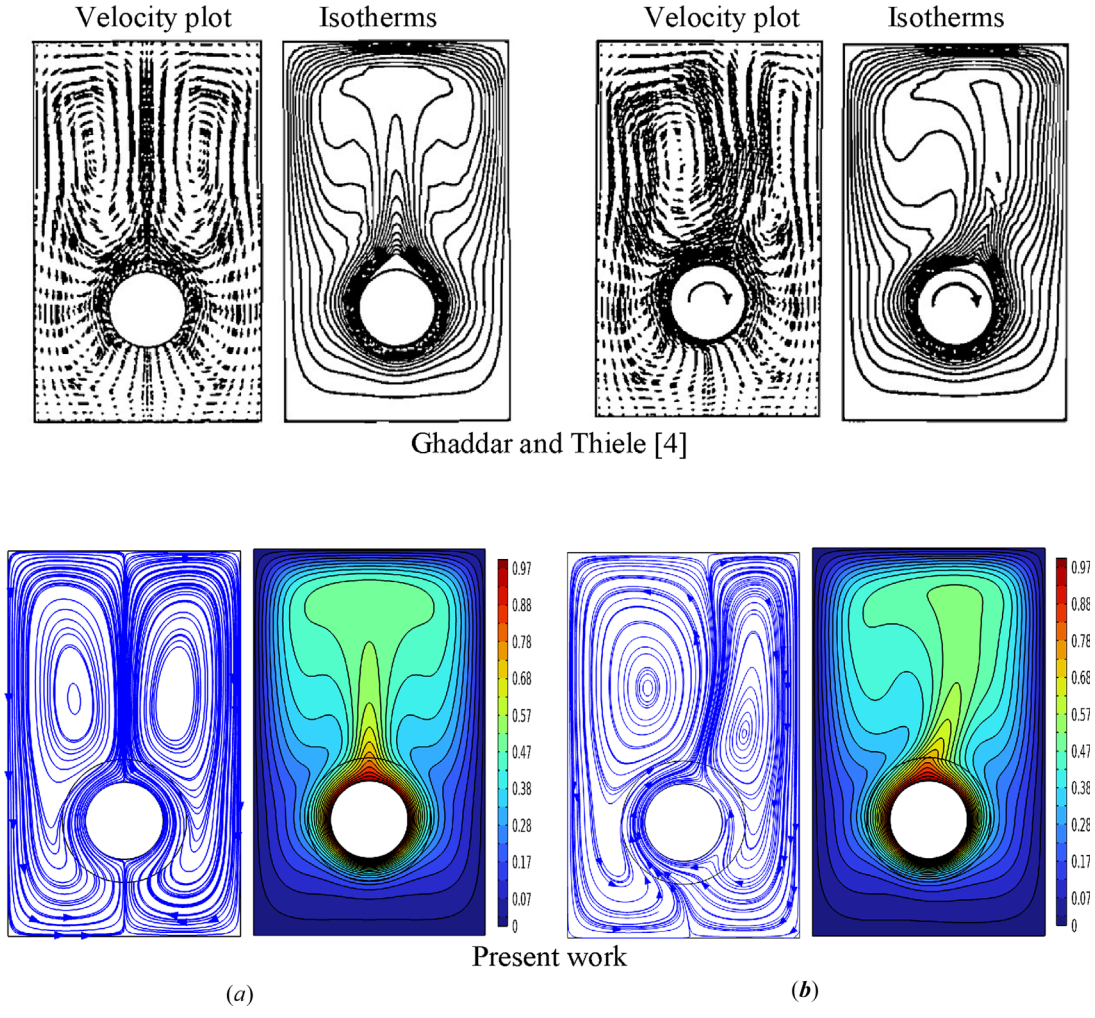

Fig. 5 Comparison with Ghaddar and Thiele [4], (*a*) at fixed cylinder Ra = 10^4 and rotational Reynold number ($\mathrm{Re}_w = 0$) and (*b*) $\mathrm{Re}_w = 15.811$ with Ra = 10^4

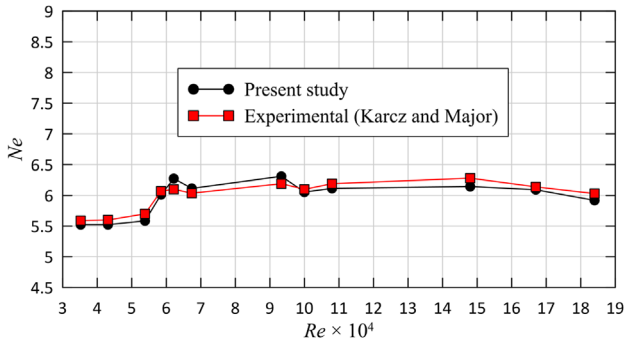

Fig. 6 Evaluation of the current research simulation and those of Karcz and Major [14], which was conducted by calculating the power consumption (Ne)

sinusoidal manner $\left(1-\frac{2\pi t}{5}\right)$. The comparison was made with the profile of the flexible base and its deflection is portrayed in Fig. 7, which shows good consistency between the two solvers. The properties of the problem are given in the caption of the figure.

4 Results and Discussions

This study defined essential dimensionless parameters: Water was chosen as the working fluid with a Prandtl number (Pr) of 6.9. The Rayleigh numbers ranged from 10^3 to 10^5, and the angular rotational speed varied between 0 and 400. It is wise to mention that the Rayleigh number accounts for the ratio of the natural convection (which is driven by the buoyancy forces) to the flow resistance (which results from the viscous forces). While the Prandtl number accounts for the ratio of the momentum diffusivity to the thermal diffusivity. The main limitations of this study are the laminar flow, which restricts the rotational speed of the frame and the fluid type that is restricted to Newtonian fluids.

In this investigation, the cold cylinders were positioned at angles $\varepsilon 1 = 22.5$ deg, 67.5 deg, 112.5 deg, and 157.5 deg, while the hot cylinders were placed at angles $\varepsilon 1 = 202.5$ deg, 247.5 deg, 292.5 deg, and 337.5 deg, with intervals of $\varepsilon 2 = 45$ deg. The length of each flexible baffle was denoted as ($a_{\text{fl.}}$) and its width as ($b_{\text{fl.}}$), evenly distributed between every two cylinders. The angle between

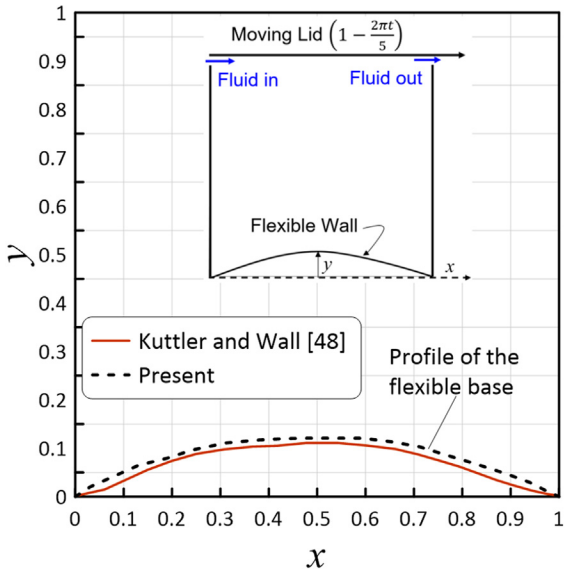

Fig. 7 FSI validation with Kuttler and Wall [48], the flexible base has: $E = 250$ N/m^2, density of 500 kg/m^3, the fluid properties are: density = 1.0 kg/m^3, dynamic viscosity = 0.01 Pa·s, while the inlet and outlet ports were 0.1 and the lid moves according to $\left(1-\frac{2\pi t}{5}\right)$

Table 1 Varying parameters utilized in this study

ω^*	Ra	r^*	e^*
0–400	10^3–10^5	0.01–0.05	0.3–0.45

the center of each cylinder and the flexible baffle was set at 22.5 deg, while the angle between each pair of flexible baffles was 45 deg.

The outcomes obtained are categorized into four sets of parameters: the first set emphasizes the distance of cylinders from the vessel center (e^*), the second set explores the effect of the rotating frame speed (ω^*), the third concerns the size of the cylinder (r^*). Finally, the fourth set compares the results in the current case with the presence of flexible baffles, the case of no baffles [34], and solid baffles. Each set of results undergoes meticulous analysis, including visualization of flow contours and isotherms and scrutiny of the heat transfer mode by computing the Nusselt number. The ranges of the parameters under investigation are outlined in Table 1. It is ensured that the maximum value of the rotational speed results in a Reynolds number $\left(\text{Re} = \frac{\omega R^* D^* \rho_f}{\mu_f}\right)$ of about 29, which is within the laminar flow range.

Particular attention is given to studying the recurring patterns of streamlines and isotherms and determining the time needed to establish a cyclical steady-state. The following subsection will detail this phenomenon:

4.1 Time-Dependent Results. The outlines in Figs. 8 and 9 delineate the streamlines and isotherms, respectively, revealing transient behaviors. Each cylinder is fixed at a radius of $r^* = 0.03$, with centers situated at a distance $e^* = 0.35$ from the vessel's center. The Rayleigh number is 10^5, with an angular speed of 400. A time-step of 0.001 is implemented to achieve higher resolution and provide a more accurate depiction of the frame's movement and the evolution of the streamlines.

Figure 8 illustrates the streamlines at the initial time of 0.001 in detail. The fluid movement and the formation of vortices commence randomly with the onset of the rotating frame's motion. This initiation involves the development of dynamic forces resulting from the predominant buoyant force, causing deviations in the baffles. Progressing in time, particularly at 0.008, an interaction is observed between the buoyant force and fluid movement, resulting in smooth streamlines, predominantly observed in the center of the frame, with stagnation areas persisting around the baffles. When the time reaches to 0.016, a prominent primary vortex forms in the direction of the rotating frame's movement, spanning the upper left and lower right quadrants, each encompassing two cold and two hot cylinders. Additionally, two smaller vortices emerge, each enveloping two identical cylinders. Stable regions of fluid movement become discernible, particularly beyond the time of 0.128, where the movement stabilizes and fluid flow becomes symmetric. Looking at the deformation states of the flexible baffles, one can deduce that a baffle guides the circulated flow into the next cylinder, and due to its flexibility, it bends with the flow direction. In a particular instant, two counter-rotating vortices are met close to the free tip of the baffles, and then the baffles reserve their straight configuration, as seen at $t^* = 0.001$ in Fig. 8.

Figure 9 illustrates that at the initial stages of the timeline, thermal plumes begin to form, albeit with insufficient speed over time, to induce natural convection effects attributed to the dominance of the buoyant force. As time progresses, a positive heat exchange is evident, represented by the large vortex surrounding the two hot and two cold cylinders, aligned with the frame's movement. Here, the interplay and equilibrium between free and forced convection become apparent, especially in the upper right and lower left quadrants, indicated by the density of thermal boundaries. The formation of two vortices around identical cylinders leads to a reduction in heat exchange. The stability of heat exchange is

highlighted by the average Nusselt number, which starts stabilizing beyond the time of 0.12, as depicted in Fig. 10.

4.2 Effect of Cylinder Size. This study primarily explores how cylinder size and flexible baffles influence temperature contours and streamlines at $t^* = 0.15$, $e^* = 0.35$, $\omega^* = 400$, and $\mathrm{Ra} = 10^5$. Notably, the velocity and buoyant force play significant roles in shaping the movement of flexible baffles. Fluid motion applies pressure on the baffles, inducing stress that affects the displacement of baffles. Consequently, the baffles deflect in the direction of fluid movement, causing the frame to rotate counterclockwise. Figure 11 displays streamlines and isotherms for the effect of cylinder diameters. When the cylinder size is small at 0.01, the deflection of baffles becomes more noticeable due to the absence of obstruction in the free surface created by the rotating frame near the baffles. This deflection adds extra momentum to the fluid particles, an FSI problem. Streamline patterns become more symmetrical and streamlined, with visible baffle movement causing compression toward the center as they pass around the cylinders. This positively impacts heat transfer, with uniform isotherms observed, indicating an enhanced heat between the mixed fluid and the baffles, thus providing an additional surface for heat exchange. Consequently, there is an increase in the contact area between the fluid and the surrounding cylinder wall. As the cylinder size increases slightly to 0.02, greater separation occurs from the previous streamlines near the cylinders. This separation is attributed to obstruction, which increases with the larger cylinder size while observing the expansion of flow in the opposite direction to the movement of the baffles. Conversely, insufficient exchange occurs between the contact surface of the cylinders and the fluid, resulting from the increased surface area of the cylinders compared to the volume of the surrounding fluid, negatively influencing the isotherms.

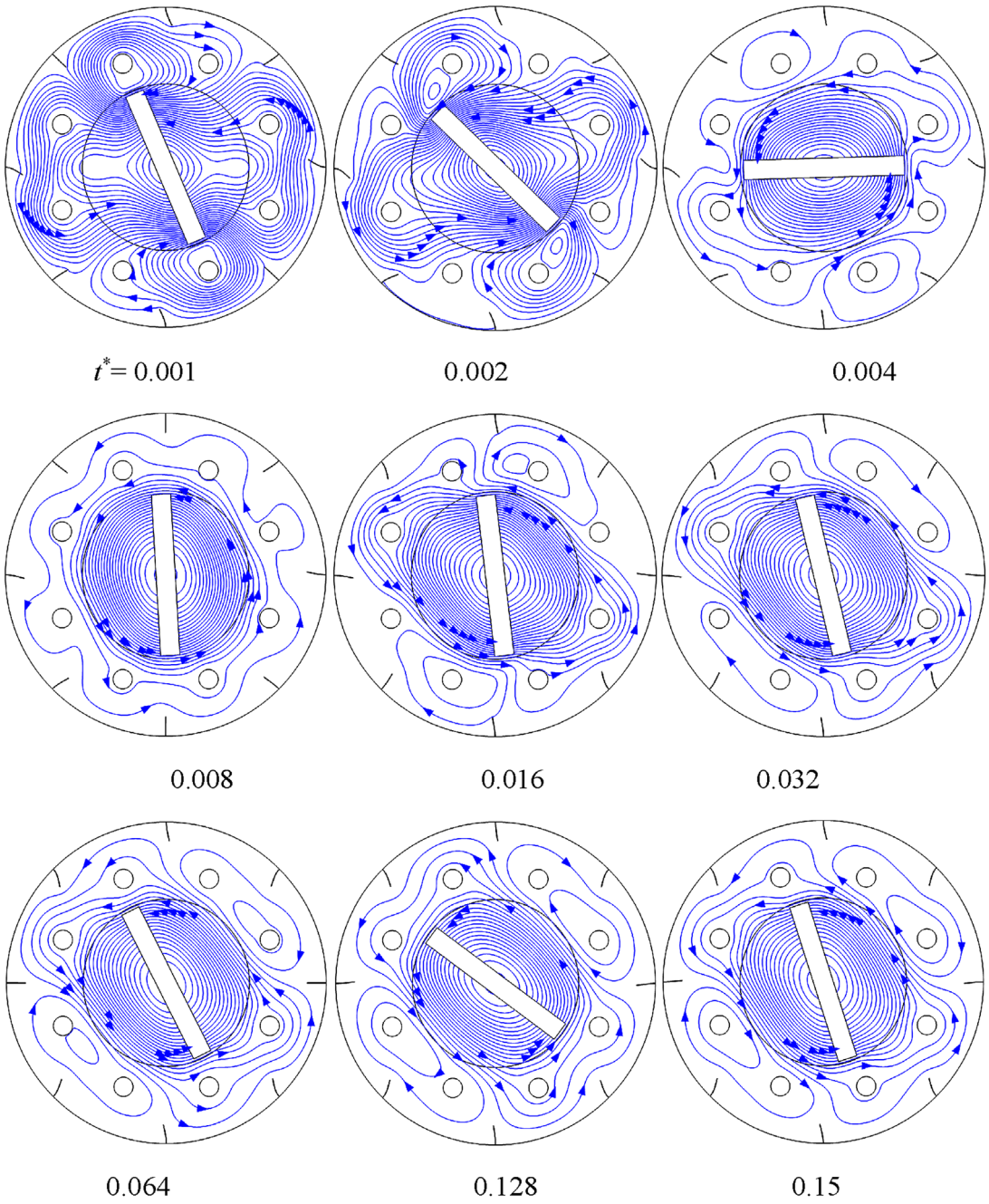

Fig. 8 Streamline contour progression was analyzed at various intervals for $e^* = 0.35$, $t^* = 0.03$, $\mathrm{Ra} = 10^5$, and $\omega^* = 400$

However, with a further increase in cylinder size to 0.05, weaknesses and distortions emerge in the flow, forming areas of slow flow surrounding the cylinders and the free surface and intermediate regions within the frame. This phenomenon is attributed to the obstruction formed due to the large size of the cylinders, acting as a buffer for the fluid movement induced by the frame. This substantial obstruction reduces exchange between the contact surface of the cylinders and the surrounding fluid, affecting baffle movement and causing them to appear stationary due to insufficient pressure for displacement. This phenomenon affects the isotherms, thickening the boundary layers and causing an uneven distribution of thermal gradients.

Figure 12 depicts the variation of the Nusselt number concerning the cylinder size alongside the rotational speed within this parameter set. The figure illustrates a consistent increase in the Nusselt number as the cylinder size decreases, with the Nusselt number experiencing a percentage increase of approximately 203.3% and 375.5% at $\omega^* = 200$ and $\mathrm{Ra} = 10^3$ and $\mathrm{Ra} = 10^5$, respectively, when the cylinder size decreases from 0.05 to 0.01. This phenomenon primarily arises from the development of consistent flow patterns around cylinders of smaller radii.

4.3 Impact of the Distance of Cylinders From the Vessel Center. These investigations examined the effects of varying the positions of the cold and hot cylinders relative to the vessel's center on streamlines and isotherms, with parameters fixed at $\mathrm{Ra} = 10^5$, $\omega^* = 400$, and $t^* = 0.15$. Figure 13 illustrates that when $e^* = 0.3$, the

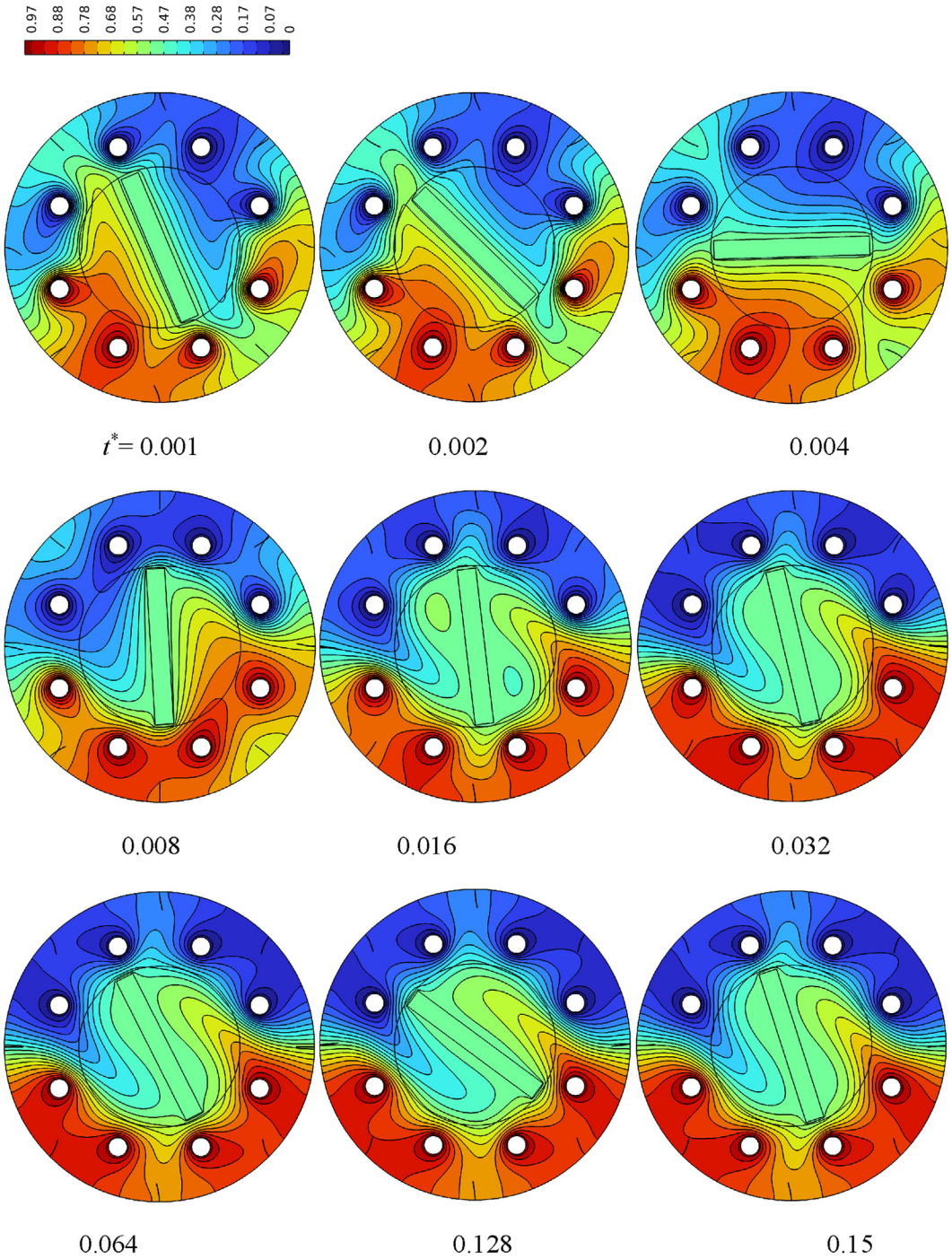

Fig. 9 Isotherms progression was analyzed at various intervals for $e^* = 0.35$, $r^* = 0.03$, $\mathrm{Ra} = 10^5$, and $\omega^* = 400$

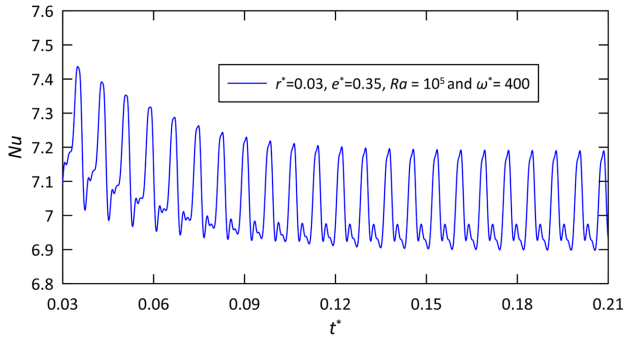

Fig. 10 Nusselt number over time, considering parameters $e^* = 0.35$, $r^* = 0.03$, $Ra = 10^5$, and $\omega^* = 400$

steep deflection of the baffle is apparent. The display highlights the smoothness of the deflection and its consistency toward the opposite direction of the rotating frame's movement. This happens because as the flexible baffles sway within the fluid, variations in pressure and velocity arise around the baffles, creating a dynamic force that opposes the direction of the baffle's movement. This shift introduces extra momentum to the streamlines and heightens the pressure within the flow, especially in the upper regions of the flexible baffles near the vessel's center. This action reduces stagnation zones around the cylinders. Conversely, in the vessel's middle, the streamlines move toward the frame's movement. When fluid collides in two areas, specifically at the cylinders located at the two corners, the fluid changes direction due to the pressure exerted by the collision, affecting the movement of the baffles. On the opposite side of the isotherms, thin thermal layers form in the middle of the rotating frame, and the reverse movement of the fluid in the area confined between the cylinders and the adiabatic surface, represented by the movement of the flexible baffles, brings the thermal plumes and mix them well with the other part.

It was also noted that the significant buoyant force and velocity propelled the hot fluid away, facilitating the mixing with the colder fluid and enhancing the thermal exchange. When the cylinders were repositioned away from the central axis of rotation to a distance of 0.4, the streamlines became denser in the upper left and lower right quadrants, creating large vortices that followed the direction of the frame's movement in those regions. This demonstrated the impact of the baffles in those areas and their movement in alignment with the frame's trajectory, influenced by the pressure exerted in those zones to generate a dynamic force for their motion. Consequently, this affected the isotherms, fostering a beneficial exchange zone where the heat plumes from the hot cylinders dispersed and mixed with those from the cold cylinders. However, in the upper right quadrant and the lower left quadrant, weak areas surrounding each of them with two identical cylinders caused stagnation areas, noting slight fluctuation in the movement of the baffles due to the lack of pressure exerted on the unit area of the baffles, leading to negative results for the isotherms. When $e^* = 0.45$, the weak areas that surrounded two identical cylinders in the previous position disappeared and became completely stagnant, with an expansion of the large vortex surrounding the outer part of the cylinders and near the source of the frame's movement. Stagnation areas were observed to the right and left, as well as nearby areas on the adiabatic surface. Here, the role of the baffles created a buffer for the movement of the fluid, compressing it toward the center and keeping it away from the cylinders, which negatively affects the isotherms. There was minimal mixing and disintegration of the thermal plume, especially

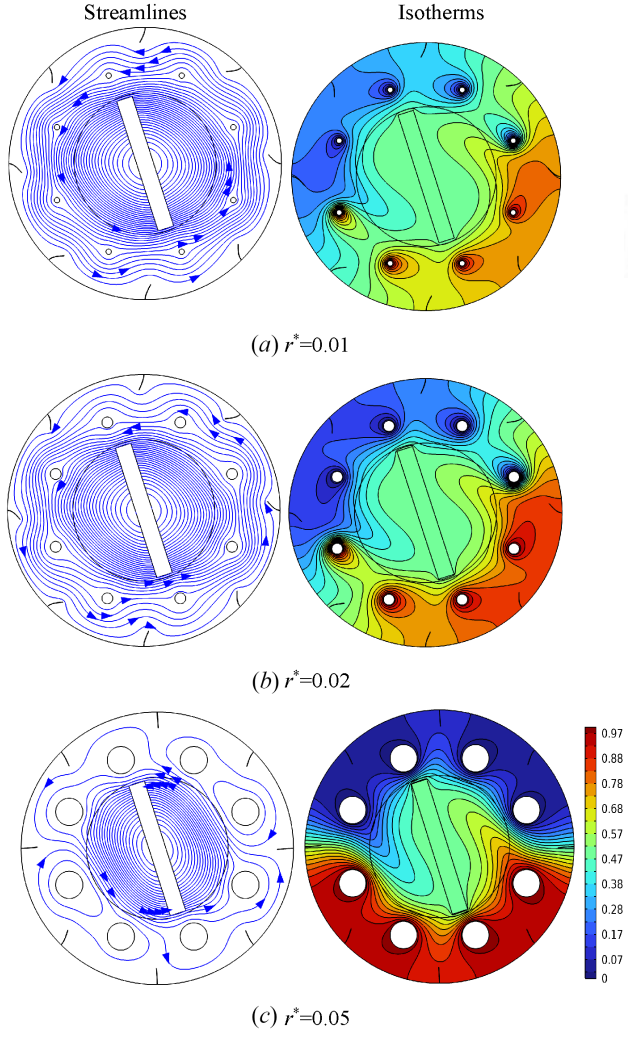

Fig. 11 Temperature contours and flow patterns at $e^* = 0.35$, $\omega^* = 400$, Ra = 10^5, and t^*=0.15, for (*a*) $r^* = 0.01$, (*b*) $r^* = 0.02$, and (*c*) $r^* = 0.05$

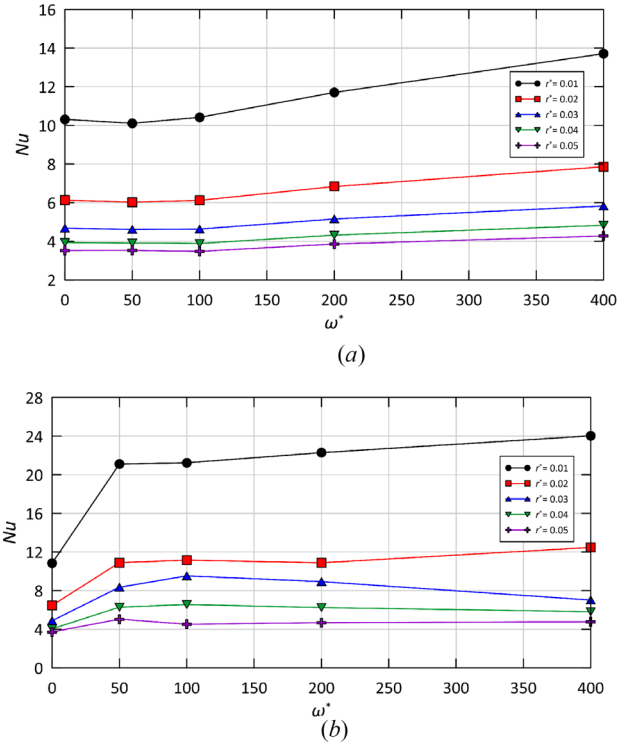

Fig. 12 The distributions of Nusselt number for (*a*) Ra = 10^3 and (*b*) Ra = 10^5 concerning rotational velocity and various cylinder radii r^*, considering $e^* = 0.35$

in the outer region corresponding to the movement of the rotating frame in the upper right and lower left quadrants.

The Nusselt number is presented in Figs. 14(*a*) and 14(*b*) for designated Ra and varying ω^*. Lower e^* values result in elevated Nusselt numbers due to two key factors. First, the reduced distance between hot and cold cylinders lowers the thermal resistance in the transfer of heat. Secondly, the nearness of the frame edges to the heated surface promotes vigorous mixing. Specifically, at $\omega^* = 200$, reducing e^* from 0.45 to 0.3 increases the Nusselt number by 72.3% and 70.26% for $\mathrm{Ra} = 10^3$ and 10^5, respectively. Moreover, it is noted that as rotational speed increases, the Nusselt number also rises, owing to enhanced fluid mixing that bolsters forced convection effects.

4.4 Impact of Rotating Frame Speed. This section emphasizes the influence of speed on streamlines and isotherms in the presence of flexible baffles. Parameters are set at $t^* = 0.15$, $e^* = 0.35$ and $r^* = 0.03$. Figure 15 represents the streamlines and isotherms relative to the effect of the rotating frame for $Ra = 10^5$. At zero speed (Fig. 15(*a*)), the streamlines are symmetric along the y-axis, and the fluid circulates in opposite direction. Following the symmetrical streamlines, the deflection state of the flexible baffles is also symmetric. The counterclockwise rotation of the right half deviates the flexible baffles in the direction of rotation due to the applied pressure. In contrast, on the left half, the streamlines rotates clockwise, with stagnation areas in the middle. This is primarily due to the dominance of the high buoyancy force, which amplifies the effect of dynamic force on the baffles, rendering them more susceptible to undulation and bending. Conversely, the buoyant force facilitates molecule movement in isotherms, enhancing thermal efficiency through pure natural convection. The disintegration of thermal layers in the hot cylinders and the resulting isothermal regions are also observed.

At $\omega^* = 100$, fluid movement intensifies, becoming multi-recirculating. In addition, the flexible baffles add a punch-like to the vortices leading to intensified mixing. This is evidenced by streamlines forming a large, symmetrical vortex along the frame's axis and direction of movement, surrounded by cold and hot cylinders. Adjacent to the large vortex, two equal differential vortices rotate opposite its direction, one enveloping a cold cylinder and two hot cylinders and the other encircling two hot cylinders and one cold cylinder. In contrast, isotherms exhibit bifurcation distribution, enhancing heat exchange between cold and hot surfaces and creating active regions in the hot zone, particularly in the lower right part where heightened movement of hotter fluid from the hot to the cold surface is observed. At $\omega^* = 400$ (Fig. 15(*c*)), identical streamlines are evident in the upper left and lower right sectors. The circulation is weakening close to the hot and cold cylinders, while intensifying in a uniform circling within the domain of the rotating frame. King et al. [49] indicated similar behavior in a rotating annular cavity. Moreover, the weak outer circulation enclose cold and hot cylinders separately. The corresponding isotherms exhibit notable plumes within the domain of the rotating frame. Hence, it is certain that at higher speed ($\omega^* = 400$), the intensifying the circulation in a region rather than the hot and cold cylinders will negatively affect the convection as can be observed in Fig. 16, where the Nusslet number of $\mathrm{Ra} = 10^5$ dwindles notable as the speed rises to 400. In general, Fig. 16 reveals that the highest value of the Nu number is recorded at Rayleigh number 10^5 at a speed of 100. At this low speed, both free convection and forced convection (due to

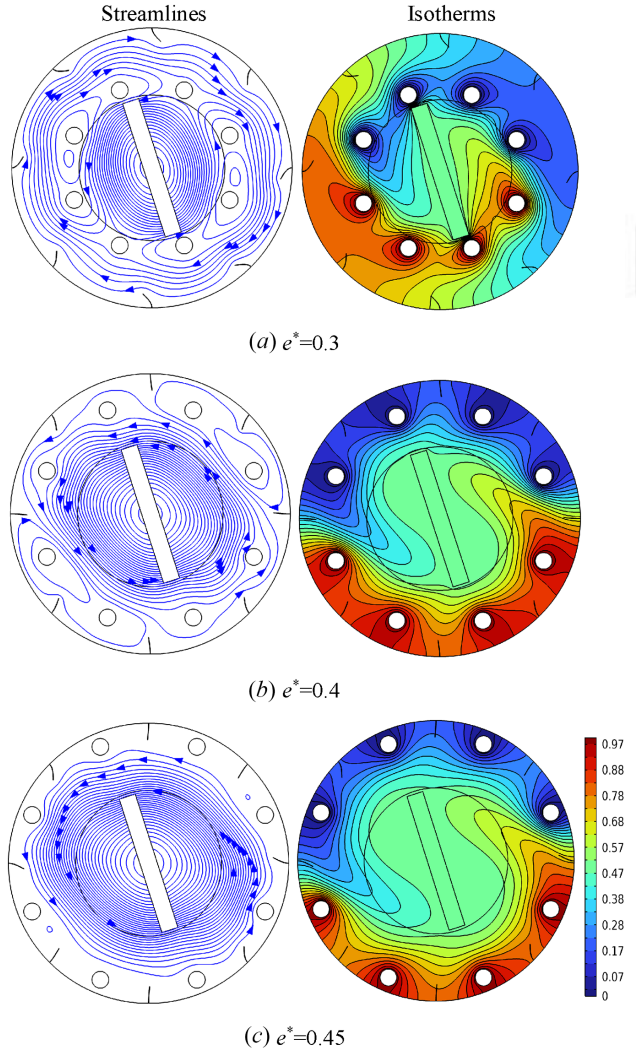

Fig. 13 Temperature contours and flow patterns at $\omega^* = 400$, $\mathrm{Ra} = 10^5$, $r^* = 0.03$, and $t^* = 0.15$, for (*a*) $e^* = 0.3$, (*b*) $e^* = 0.4$, and (*c*) $e^* = 0.45$

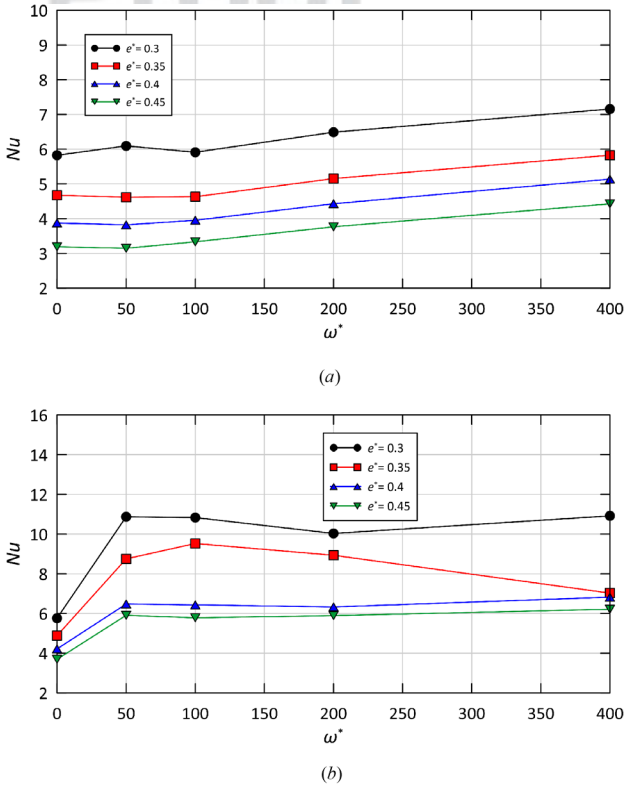

Fig. 14 Nusselt number variation with rotational velocity for various distances of the cylinders from the rotating frame at (*a*) $\mathrm{Ra} = 10^3$ and (*b*) $\mathrm{Ra} = 10^5$, for $r^* = 0.03$

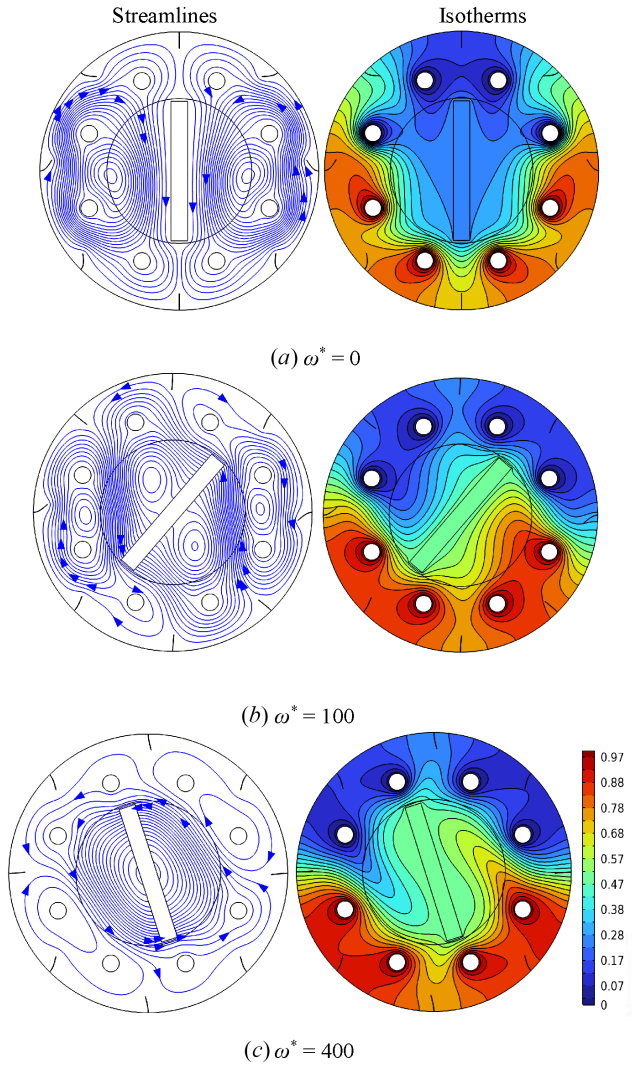

Fig. 15 Temperature contours and flow patterns for $e^* = 0.35$, $t^* = 0.15$, Ra = 10^5, and $r^* = 0.03$ at rotational velocities (*a*) $\omega^* = 0$, (*b*) $\omega^* = 100$, and (*c*) $\omega^* = 400$

631 rotation) are comparable. However, at lower Rayleigh numbers
632 where rotation plays a more significant role, we observe that
633 increasing the rotation consistently raises the Nusselt number, albeit
634 by a small percentage. Commonly, with an increase in rotational
635 speed from zero to 200, there is an observed rise in the Nu of 10.2%
636 and 82.9% for Ra = 10^3 and 10^5, respectively. Hence, the higher
637 rotational speed is not recommended at high Ra number, as the fluid
638 circulation of higher rotational speed is limited in a region far from

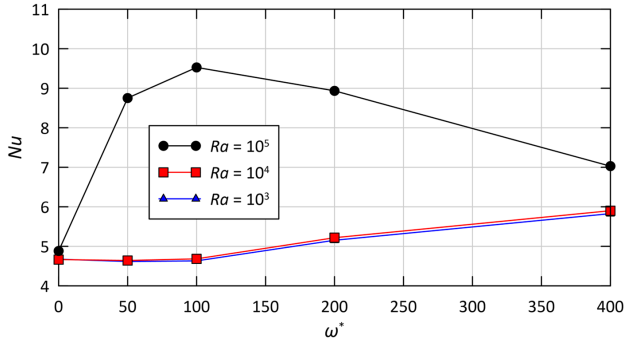

Fig. 16 The distribution of the Nusselt number with rotational speed for various Ra, considering $r^* = 0.03$ and $e^* = 0.35$

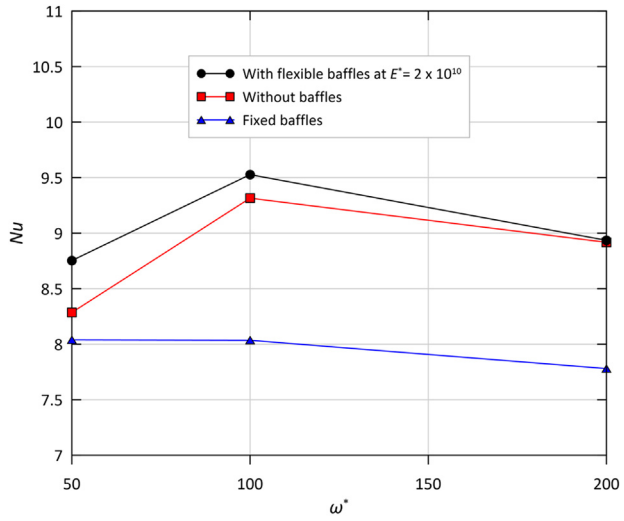

Fig. 17 Comparison between the elastic baffles, fixed baffles, and without baffles [45] for Nusselt number variation with the ω^* for r^*=0.03, Ra = 10^5, and e^*=0.35

Table 2 The increase of the Nusselt number when using flexible baffles at $e^* = 0.35$, Ra = 10^5, and $r^* = 0.03$

Speed (ω^*)	The increase in Nu for flexible baffles compared with no baffles	The increase in Nu for flexible baffles compared with rigid baffles
50	5.64%	8.8%
100	2.27%	18.5%
200	0.2%	14.84%

the cylinders, which are kept at different temperatures, the fact that 639
declared previously by King et al. [49]. 640

4.5 Comparative Study. In this section, comparing the current 641
investigation involving flexible baffles with a previous study [34], 642
which has no baffles, is conducted. Furthermore, a comparison with 643
fixed baffles is incorporated by analyzing Nusselt number 644
distribution and skin friction number. 645

Figure 17 compares Nusselt number distribution at various speeds 646
with other parameters fixed at $r^* = 0.03$, Ra = 10^5, and $e^* = 0.35$. 647

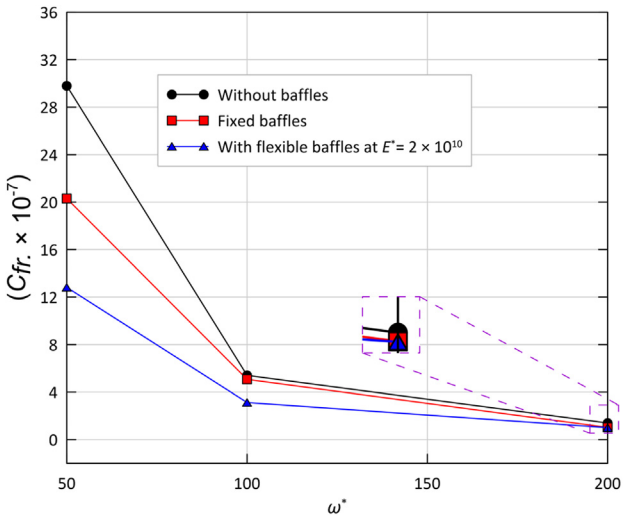

Fig. 18 Comparison between the elastic baffles, fixed baffles, and without baffles [34] for Skin friction number distribution with the rotational speed for $r^* = 0.03$, Ra = 10^5, and $e^* = 0.35$

Table 3 The declination of skin friction when using flexible baffles at $e^* = 0.35$, Ra = 10^5, and $r^* = 0.03$

Speed (ω^*)	The reduction in C_{fr} for flexible baffles compared with no baffles	The reduction in C_{fr} for flexible baffles compared with rigid baffles
50	56.9%	36.84%
100	42.2%	38.39%
200	27.9%	1.97%

Table 4 The increase of the Performance coefficient when using flexible baffles and compared to fixed baffle at $e^* = 0.35$, Ra = 10^5, and $r^* = 0.03$

Speed (ω^*)	The increase in Pf for flexible baffles compared with rigid baffles
50	72.41%
100	92.48%
200	17.15%

The study elucidates the impact of speed on the three configurations. At lower speeds, particularly at 50, the influence of flexible baffles on the Nusselt number is evident, exhibiting a 5.64% increase compared to the absence of baffles. This disparity can be attributed to the domination of buoyant force relative to speed, affecting baffle deflection. With its relatively minor deformation, flexible baffles prove more effective in heat exchange by enhancing heat circulation between cold and hot cylinders. However, as speed increases, adverse outcomes are observed for the flexible baffle configuration compared to the other cases. This is due to heightened fluid movement inducing significant distortions in the fluid stream due to baffle shape alteration, leading to increased dynamic and frictional pressure and resulting in a reduced heat transfer compared to the baffle less configuration. Compared to the fixed baffles, the Nusselt number shows a noticeable increase of 8.8%, 18.5%, and 14.84% at 50, 100, and 200 speeds, respectively. Table 2 illustrates the increase in Nu number when using flexible baffles and compress the results with no baffles case and solid baffles.

In the second case, depicted in Fig. 18, the skin friction coefficient is calculated using the parameters aforementioned for the three configurations. This coefficient is crucial for optimizing design and enhancing efficiency and performance, particularly in mixing operations. Flexible baffles have a significant impact across various speeds, with a peak decrease of 56.9% at ($\omega^* = 50$) compared to no baffle case and a decrease of 38.39% at ($\omega^* = 100$) compared to fixed baffles. Their presence reduces friction between fluid molecules and the surface, decreasing the shear stress. Consequently, this reduction in shear stress diminishes the total system load, enhancing its efficiency and performance. Table 3 illustrates the declination in skin friction for flexible baffles compared to the other configurations at different speeds.

Conversely, Fig. 19 illustrates the performance coefficient for different speeds with fixed values of $r^* = 0.03$, Ra = 10^5, and $e^* = 0.35$. The performance coefficient for the flexible baffle reached its maximum at a speed of 50. This is due to the increase in the Nusselt number when flexible baffles are used, compared to their absence, and a significant reduction in the skin friction coefficient. However, as speed increases further, the performance coefficient begins to decrease. Additionally, it is noted that the coefficient rises at a speed of 100, peaking at 92.48% when comparing the performance with flexible baffles to that with fixed baffles. Table 4 shows the increase in performance coefficient at different speeds for flexible baffles compared to fixed baffles under the same conditions.

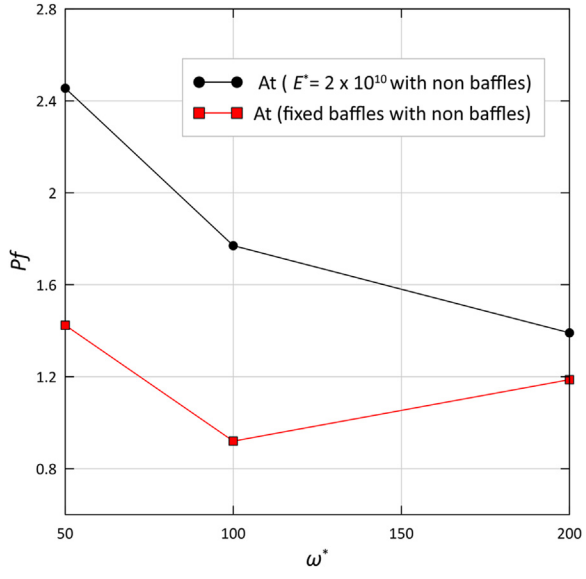

Fig. 19 Performance coefficient with different speeds when the parameters are constant at $e^* = 0.35$, Ra = 10^5, and $r^* = 0.03$

5 Conclusions

Heat exchange between the cylinders within a vessel is enhanced by employing a rotating frame and flexible baffles. This paper undertakes a numerical investigation of this problem. The study parameterizes the distance, size, and rotational speed and compares them with nonbaffle and solid baffle configurations, utilizing varying Rayleigh numbers for comprehensive analysis. The findings reveal that the distance, size, and rotational speed notably affect heat transfer within the system, underscoring their significance in designing container and tube heat exchangers. The key findings are summarized succinctly as follows:

- As the frame's rotational speed increases, Nusselt number increases also; however, its effectiveness diminishes after surpassing a critical rotational speed of $\omega^* = 200$ due to increased drag and flow disruption around the cylinders. Notably, the Nusselt number grows by 82.9% and 10.2% for Ra = 10^5 and 10^3, respectively, when ω^* increases from zero to 200.
- The Nusselt number rises, as the cylinders are closer to the rotating frame. Specifically, decreasing the distance of the cylinders from the rotational frame from $e^* = 0.45$ to 0.3 results in a Nu number enhancement of 72.3% at Ra = 10^3 and 70.26% at Ra = 10^5 at ω^*=200.
- Reducing the cylinder size increases the Nusselt number, influenced by the temperature differentials and drag effects. Specifically, the Nu increases by 375.5% and 203.3% for Ra = 10^5 and Ra = 10^3, respectively, at $\omega^* = 200$ when the cylinder size is reduced from $r^* = 0.05$ to $r^* = 0.01$.
- When compared to fixed baffles, flexible baffles yield increases in the Nusselt number of 8.8%, 18.5%, and 14.84% at speeds of 50, 100, and 200, respectively.

This study has a limitation due to the relatively low rotational speed. Increasing the rotational speed into the turbulent range could reveal new functions of the flexible baffles. Therefore, the issue of turbulence warrants further investigation in future research.

Conflict of Interest

The authors declare that there are no conflicts of interest.

Nomenclature

a = length, m
A = oscillation amplitude, m
b = width, m
$C_{fr.}$ = skin friction, dimensionless
C_p = specific heat, J kg^{-1} K^{-1}

D = vessel diameter (2R), m
$d_{\text{fl.}}$ = displacement, m
Di = agitator diameter, m
e = distance between the cylinder to the vessel center, m
E = elastic modulus, N m^{-2}
$\mathbf{F}_b$ = vector of body force, N m^{-3}
k = thermal conductivity, Wm^{-1} K^{-1}
k_r = the conductivity ratio between the solid (flexible baffle) and fluid
Mt = torque, N·m
n = unity normal vector
N = number of cylinders
Nct = count of cold cylinders
Nht = count of hot cylinders
Ne = power consumption, dimensionless
Nu = Nusselt number, dimensionless
p = field of pressure, N m^{-2}
Pf = coefficient of performance, dimensionless
Pr = Prandtl number
Po = power consumption, W
r = Cylinders radius, m
R = Vessel's radius, m
Ra = number of Rayleigh, dimensionless
Re = Reynold number, dimensionless
R_h = ratio of heat capacity
$R_{\text{th.}}$ = ratio of thermal conductivity
t = time, s
T = temperature, K
t_p = oscillation period, s
u, v = velocity of fluid, m s^{-1}
$\mathbf{V}$ = velocity vector (absolute), m s^{-1}
$\mathbf{W}$ = velocity vector (relative), m s^{-1}
$\mathbf{W}_{\text{co}}$ = component velocity vector, $\mathbf{W}_{\text{co.}} = \mathbf{W} - \mathbf{W}_{\text{fl.}}$, m s^{-1}
$\mathbf{W}_{\text{fl}}$ = the velocity vector of the moving coordinate, m s^{-1}

Greek Symbols

α = diffusivity of thermal, m^2 s^{-1}
β = fluid's thermal expansion coefficient, K^{-1}
ε = the angle of the cylinder position
θ = nondimensional temperature, $\theta = \frac{(T-T_h)}{(T_c-T_h)}$
μ = dynamic viscosity, kg m^{-1} s^{-1}
ρ = density, kg m^{-3}
υ = fluid's kinematic viscosity, m^2 s^{-1}
$\omega, \boldsymbol{\omega}$ = frame's angular velocity, vector, rad s^{-1}
ω_i = agitator speed, s^{-1}

Subscripts

baf = baffles
c = cold
f = fluid
fl = flexible baffle
h = hot
j = vector unit aligned with the y-axis
s = solid
o = reference value

Supersubscripts

$*$ = dimensionless

References

[1] Dominguez-Ontiveros, E., and Hassan, Y. A., 2014, "Experimental Study of a Simplified 3 × 3 Rod Bundle Using DPTV," Nucl. Eng. Des., **279**, pp. 50–59.
[2] Azzouz, R., and Hamida, M. B. B., 2023, "Natural Convection in a Circular Enclosure With Four Cylinders Under Magnetic Field: Application to Heat Exchanger," Processes, **11**(8), p. 2444.
[3] Machi, M. H., Farkas, I., and Buzas, J., 2024, "Enhancing Solar Air Collector Performance Through Optimized Entrance Flue Design: A Comparative Study," Int. J. Thermofluids, **21**, p. 100561.
[4] Ghaddar, N., and Thiele, F., 1994, "Natural Convection Over a Rotating Cylindrical Heat Source in a Rectangular Enclosure," Numer. Heat Transf., **26**(6), pp. 701–717.
[5] Kimura, T., Takeuchi, M., Nagai, N., and Yoshida, T., 2003, "Heat Transfer Control in an Enclosure Using a Rotating Plate and Stratified Fluids," Heat, Transfer Asian Res., **32**(6), pp. 489–500.
[6] Paramane, S. B., and Sharma, A., 2009, "Numerical Investigation of Heat and Fluid Flow Across a Rotating Circular Cylinder Maintained at Constant Temperature in 2-D Laminar Flow Regime," Int. J. Heat Mass Transfer, **52**(13–14), pp. 3205–3216.
[7] Costa, V., and Raimundo, A., 2010, "Steady Mixed Convection in a Differentially Heated Square Enclosure With an Active Rotating Circular Cylinder," Int. J. Heat Mass Transfer, **53**(5–6), pp. 1208–1219.
[8] Hussain, S. H., and Hussein, A. K., 2011, "Mixed Convection Heat Transfer in a Differentially Heated Square Enclosure With a Conductive Rotating Circular Cylinder at Different Vertical Locations," Int. Commun. Heat Mass Transfer, **38**(2), pp. 263–274.
[9] Liao, C.-C., and Lin, C.-A., 2014, "Mixed Convection of a Heated Rotating Cylinder in a Square Enclosure," Int. J. Heat Mass Transfer, **72**, pp. 9–22.
[10] Chatterjee, D., Gupta, S. K., and Mondal, B., 2014, "Mixed Convective Transport in a Lid-Driven Cavity Containing a Nanofluid and a Rotating Circular Cylinder at the Center," Int. Commun. Heat Mass Transfer, **56**, pp. 71–78.
[11] Atanasova, G., Ducci, A., and Micheletti, M., 2024, "Fluid Dynamics and Mixing in a Novel Intermittently Rotating Bioreactor for CAR-T Cell Therapy: Spin-Down From Incomplete Spin-Up," Chem. Eng. Res. Des., **205**, pp. 486–497.
[12] Mokhefi, A., 2024, "Hydrodynamic and Thermal Performance Analysis of an Inclined Anchor Impeller Designed for Yield Stress Food Mixing Applications," Food Bioprod. Process., **143**, pp. 255–270.
[13] Yin, Y., Huang, K., Su, B., Lin, M., and Wang, Q., 2024, "Experimental Study on the Flow Mixing in T-Junctions With an Impeller," Phys. Fluids, ■(■), p. 36. AQ8
[14] Karcz, J., and Major, M., 1998, "An Effect of a Baffle Length on the Power Consumption in an Agitated Vessel," Chem. Eng. Process., **37**(3), pp. 249–256.
[15] Promvonge, P., Sripattanapipat, S., Tamna, S., Kwankaomeng, S., and Thianpong, C., 2010, "Numerical Investigation of Laminar Heat Transfer in a Square Channel With 45° Inclined Baffles," Int. Commun. Heat Mass Transfer, **37**(2), pp. 170–177.
[16] Sriromreun, P., Thianpong, C., and Promvonge, P., 2012, "Experimental and Numerical Study on Heat Transfer Enhancement in a Channel With Z-Shaped Baffles," Int. Commun. Heat Mass Transfer, **39**(7), pp. 945–952.
[17] Xia, D., Mao, Z., Zhou, S., He, X., and Wang, Y., 2023, "Optimized Design of Solid–Liquid Dual-Impeller Mixing Systems for Enhanced Efficiency," ACS Omega, **8**(50), pp. 47635–47645.
[18] Al-Amiri, A., and Khanafer, K., 2011, "Fluid-Structure Interaction Analysis of Mixed Convection Heat Transfer in a Lid-Driven Cavity With a Flexible Bottom Wall," Int. J. Heat Mass Transfer, **54**(17–18), pp. 3826–3836.
[19] Engel, M., and Griebel, M., 2009, "Flow Simulation on Moving Boundary-Fitted Grids and Application to Fluid-Structure Interaction," Int. J. Numer. Methods Eng., **78**(■), pp. 980–1012.
[20] Shi, X., and Khodadadi, J., 2004, "Fluid Flow and Heat Transfer in a Lid-Driven Cavity Due to an Oscillating Thin Fin: Transient Behavior," ASME J. Heat Mass Transfer-Trans. ASME, **126**(6), pp. 924–930.
[21] Gomes, J. P., and Lienhart, H., 2013, "Fluid-Structure Interaction-Induced Oscillation of Flexible Structures in Laminar and Turbulent Flows," J. Fluid Mech., **715**, pp. 537–572.
[22] Ku, C.-H., 2015, "Flexible Heat Transfer Assembly," U.S. Patent Application No. 14/084,284.
[23] Soti, A. K., Bhardwaj, R., and Sheridan, J., 2015, "Flow-Induced Deformation of a Flexible Thin Structure as a Manifestation of Heat Transfer Enhancement," Int. J. Heat Mass Transfer, **84**, pp. 1070–1081.
[24] Ghalambaz, M., Jamesahar, E., Ismael, M. A., and Chamkha, A. J., 2017, "Fluid-Structure Interaction Study of Natural Convection Heat Transfer Over a Flexible Oscillating Fin in a Square Cavity," Int. J. Therm. Sci., **111**, pp. 256–273.
[25] Saleh, H., Siri, Z., and Hashim, I., 2019, "Role of Fluid-Structure Interaction in Mixed Convection From a Circular Cylinder in a Square Enclosure With Double Flexible Oscillating Fins," Int. J. Mech. Sci., **161-162**, p. 105080.
[26] Mahmood, F. T., Das, A., Smriti, R. B., Hakim, M. A., Saha, S., and Hasan, M. N., 2023, "Role of Wall-Mounted Flexible Flow Modulator on Thermo-Hydraulic Characteristics of Pulsating Channel Flow," Results Eng., **17**, p. 100941.
[27] Roy, P. P., Chowdhury, S., Raj, M. H., Islam, M. Q., and Saha, S., 2023, "Forced, Natural and Mixed Convection of Non-Newtonian Fluid Flow in a Square Chamber With Moving Lid and Discrete Bottom Heating," Results Eng., **17**, p. 100939.
[28] Mahmood, F. T., Chowdhury, T. S., and Hasan, M. N., 2024, "Fluid-Structure Interaction Induced Mixed Convection Characteristics in a Lid-Driven Square Cavity With Non-Newtonian Power-Law Fluids," Int. J. Thermofluids, **22**, p. 100687.
[29] Alsabery, A. I., Ismael, M. A., Chamkha, A. J., and Hashim, I., 2018, "Numerical Investigation of Mixed Convection and Entropy Generation in a Wavy-Walled Cavity Filled With Nanofluid and Involving a Rotating Cylinder," Entropy, **20**(9), p. 664.
[30] Sheremet, M. A., Oztop, H. F., Pop, I., and Abu-Hamdeh, N., 2015, "Analysis of Entropy Generation in Natural Convection of Nanofluid Inside a Square Cavity Having Hot Solid Block: Tiwari and Das' Model," Entropy, **18**(1), p. 9.
[31] Bondareva, N. S., Sheremet, M. A., Oztop, H. F., and Abu-Hamdeh, N., 2017, "Entropy Generation Due to Natural Convection of a Nanofluid in a Partially Open Triangular Cavity," Adv. Powder Technol., **28**(1), pp. 244–255.
[32] Sheremet, M. A., Pop, I., Oztop, H. F., and Abu-Hamdeh, N., 2017, "Natural Convection of Nanofluid Inside a Wavy Cavity With Non-Uniform Heating: Entropy Generation Analysis," Int. J. Numer. Methods Heat Fluid Flow, **27**, pp. 958–980.

[33] Hashim, I., Alsabery, A. I., Sheremet, M. A., and Chamkha, A. J., 2019, "Numerical Investigation of Natural Convection of Al_2O_3-Water Nanofluid in a Wavy Cavity With Conductive Inner Block Using Buongiorno's Two-Phase Model," Adv. Powder Technol., **30**(2), pp. 399–414.

[34] Abd Al-Hasan, A. Q., Ismael, M. A., and Ghalambaz, M., 2024, "Heat Transfer in a Vessel-Tubes Array With a Rotating Baffle: A Rotating Frame Modeling Approach," Int. J. Thermofluids, **22**, p. 100659.

[35] Wu, K., Huang, F., and Shen, J., 2022, "A New Class of Higher-Order Decoupled Schemes for the Incompressible Navier-Stokes Equations and Applications to Rotating Dynamics," J. Comput. Phys., **458**, p. 111097.

[36] Menon, S. H., Rao A, R., Mathew, J., and J, J., 2021, "Derivation of Navier–Stokes Equation in Rotational Frame for Engineering Flow Analysis," Int. J. Thermofluids, **11**, p. 100096.

[37] Ali, F., Murtaza, S., Sheikh, N. A., and Khan, I., 2019, "Heat Transfer Analysis of Generalized Jeffery Nanofluid in a Rotating Frame: Atangana–Baleanu and Caputo–Fabrizio Fractional Models," Chaos Solitons Fractals, **129**, pp. 1–15.

[38] Mohammed, E. G., and Abood, F. A., 2022, "Numerical Study Mixed Convection in a Channel With an Open Cavity Involving Rotary Cylinder," Basrah J. Eng. Sci., **22**(1), pp. 20–28.

[39] Bonet, J., and Wood, D., 1997, *Nonlinear Continuum Mechanics for Finite Element Analysis*, Cambridge University Press, ■.

[40] Shih, Y.-C., Khodadadi, J., Weng, K.-H., and Ahmed, A., 2009, "Periodic Fluid Flow and Heat Transfer in a Square Cavity Due to an Insulated or Isothermal Rotating Cylinder," Int. J. Therm. Sci., **48**(■), pp. 1965–1976.

[41] Schenk, O., and Gärtner, K., 2004, "Solving Unsymmetric Sparse Systems of Linear Equations With PARDISO," Future Gener. Comput. Syst., **20**(3), pp. 475–487.

[42] Wriggers, P., 2008, *Nonlinear Finite Element Methods*, Springer, ■.

[43] Verbosio, F., De Coninck, A., Kourounis, D., and Schenk, O., 2017, "Enhancing the Scalability of Selected Inversion Factorization Algorithms in Genomic Prediction," J. Comput. Sci., **22**, pp. 99–108.

[44] Bollhöfer, M., Eftekhari, A., Scheidegger, S., and Schenk, O., 2019, "Large-Scale Sparse Inverse Covariance Matrix Estimation," SIAM J. Sci. Comput., **41**(1), pp. A380–A401.

[45] Bollhöfer, M., Schenk, O., Janalik, R., Hamm, S., and Gullapalli, K., 2020, "State-of-the-Art Sparse Direct Solvers," Parallel Algor. Comput. Sci. Eng., ■(■), pp. 3–33.

[46] Schenk, O., and Gärtner, K., 2011, "Pardiso," *Encyclopedia of Parallel Computing*, D. Padua, ed., Springer, Boston, MA.

[47] Tarannum, F., Danayat, S., Nayal, A., Muthaiah, R., Annam, R. S., and Garg, J., 2023, "Thermally Expanded Graphite Polyetherimide Composite With Superior Electrical and Thermal Conductivity," Mater. Chem. Phys., **298**, p. 127404.

[48] Küttler, U., and Wall, W. A., 2008, "Fixed-Point Fluid–Structure Interaction Solvers With Dynamic Relaxation," Comput. Mech., **43**(1), pp. 61–72.

[49] King, M. P., Wilson, M., and Owen, J. M., 2007, "Rayleigh-Bénard Convection in Open and Closed Rotating Cavities," ASME J. Eng. Gas Turbines Power, **129**(2), pp. 305–311.